Micro-Gyroscopes with Dynamic Disturbance Rejection

Cenk Acar and Andrei M. Shkel

Microsystems Laboratory, Department of Mechanical and Aerospace Engineering
University of California at Irvine, CA, USA

ABSTRACT

This paper reports a novel micromachined gyroscope design with inherent disturbance-rejection capabilities. The proposed approach is based on increasing the degrees-of-freedom (DOF) of the oscillatory system by the use of two independently oscillating proof masses. Utilizing dynamical amplification in the 4-DOF system, inherent disturbance rejection is achieved, providing reduced sensitivity to structural and thermal parameter fluctuations and damping changes over the operating time of the device. In the proposed system, the first mass is forced to oscillate in the drive direction, and the response of the second mass in the orthogonal direction is sensed. The response has two resonant peaks and a flat region between peaks. Operation is in the flat region, where the gain is insensitive to frequency fluctuations. Simulations indicate over 15 times increase in the bandwidth of the system due to the use of the proposed architecture. In addition, the gain in the operation region has low sensitivity to damping changes. Consequently, by utilizing the disturbance-rejection capability of the dynamical system, improved robustness is achieved, which can relax tight fabrication tolerances and packaging requirements and thus result in reducing production cost of micromachined gyroscopes.

Keywords: MEMS, inertial sensors, micromachined gyroscopes, disturbance rejection.

1. INTRODUCTION

With the advances in micromachining technologies, low cost, on-chip inertial micro-sensors are beginning to enter the market. Derived from the conventional Integrated Circuit (IC) fabrication technologies, micromachining processes allow mass-production of microstructures with moving bodies on a chip together with control and signal conditioning electronics. Thus expensive and bulky conventional inertial sensors will be eventually replaced by their micromachined counterparts without compromising performance. Likewise, micromachined gyroscopes could potentially provide high accuracy rotation measurements leading to a wide range of applications including navigation and guidance systems, automotive safety systems, and consumer electronics. Gyroscopes are probably the most challenging type of transducers ever attempted to be designed using MEMS technology. Due to complexity of their dynamics, the current state of the art micromachined gyroscopes require an order of magnitude improvement in performance, stability, and robustness.

All existing micromachined rate gyroscopes operate on the vibratory principle of a single proof mass suspended by flexures anchored to the substrate. The flexures serve as the flexible suspension between the proof mass and the substrate, making the mass free to oscillate in two orthogonal directions - the drive and the sense[1] (Fig. 2a). The proof mass is driven into resonance in the drive direction by an external sinusoidal force with a certain drive frequency. If the gyroscope is subjected to an angular rotation, the Coriolis force is induced in the y-direction. The resulting oscillation amplitude in the sense direction is proportional to the Coriolis force, and thus to the angular velocity to be measured.[3]

To achieve the maximum possible gain, the conventional gyroscopes are designed to operate at the peak of the response curve. This is typically achieved by matching drive and sense resonant frequencies (Fig. 2b). However, the system is very sensitive to variations in system parameters causing a shift in the resonant frequency. For example, a 1% fluctuation in frequency matching between drive and sense modes will produce an error of 20% in the output signal gain.[4] Under high quality factor conditions the gain is high, however the bandwidth is extremely narrow. In addition, the gain is affected significantly by fluctuations in damping conditions (Fig. 2b).

Further author information: (Send correspondence to C.A.)
C.A.: E-mail: cacar@uci.edu
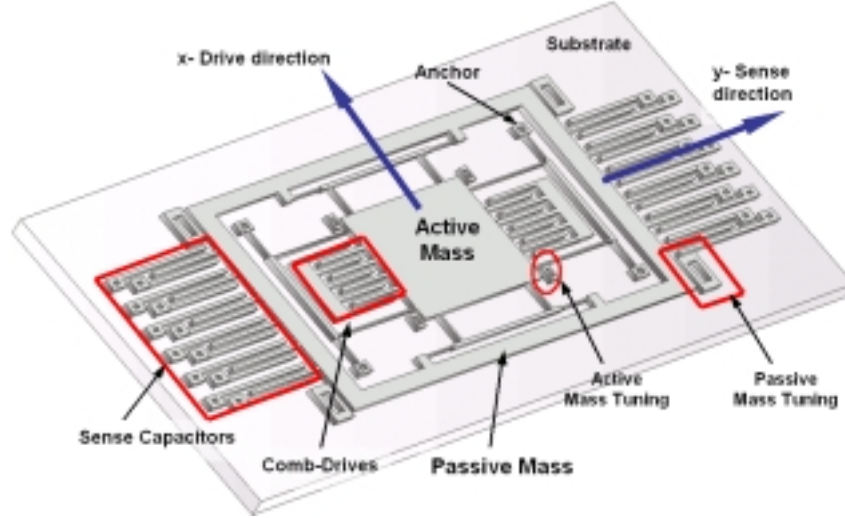A.S.: E-mail: ashkel@uci.edu
Web: http://mems.eng.uci.edu

Figure 1. Illustration of the proposed dual-mass z-axis gyroscope.

Fabrication imperfections are inevitable, and affect material properties and geometry of MEMS structures. For surface micromachining, the thickness of the suspension elements is determined by deposition process, and the width is affected by etching process. In addition, Young's Modulus of the structure is affected by deposition conditions. Variations in elastic modulus, beam thickness or residual stresses have drastic effects on resonant frequencies of gyroscopes. Generally, very sophisticated control electronics is used to provide operation in the region of the resonance peak.[6] Furthermore, during the operation time of these devices, fluctuations in the ambient temperature alter the gyroscope geometry together with structural properties, and pressure fluctuations affect the damping conditions; resulting in significant errors.

To eliminate the limitations of the existing micromachined gyroscopes, a design approach that does not require the system to operate in resonance is presented in this paper. The proposed architecture suggests the use of two independently vibrating proof masses in the dynamical system (Fig. 1) instead of one, as this is typically done in the conventional devices. The first mass is forced to oscillate in the drive direction, and this forced oscillation is amplified by the second mass. The response of the second mass in the orthogonal sense direction is monitored. The resulting 4-DOF dynamic system has a more favorable frequency response, and can operate in a wider frequency band with insignificant change in the gain. The device is demonstrated to have improved robustness against expected fabrication and packaging fluctuations, especially against damping variations due to ambient pressure. The sensitivity of performance to fabrication variations, and to temperature and pressure changes are presented in the "Parametric Sensitivity Analysis" section.
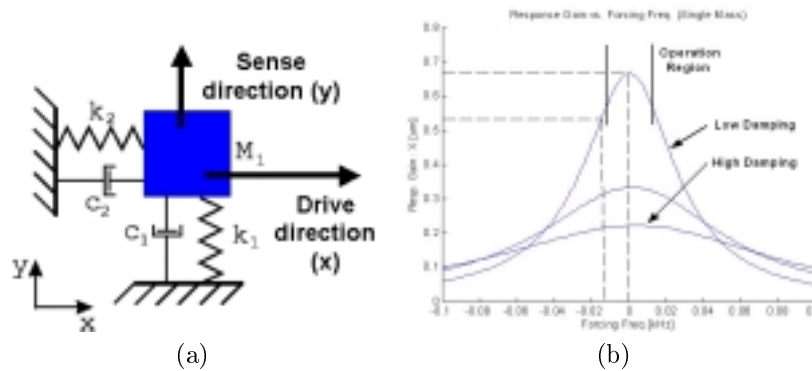

(a)   (b)

Figure 2. (a) A conventional rate gyroscope has a single proof mass which is free to oscillate in two principle directions: drive and sense. (b) The response of the system can be viewed as a 1-DOF system excited by the Coriolis force. Note that the gain is very sensitive to drive and sense mode resonant frequency matching variations and damping fluctuations.

2. THE DUAL-MASS DESIGN APPROACH

In contrast to the conventional gyroscopes that operate in resonance mode to achieve high gain, the proposed approach utilizes dynamic amplification of mechanical motion without requiring the system to operate in resonance. In order to achieve dynamic amplification, a system containing two vibrating proof masses (Fig. 3) is used. Moreover, the increased design parameter space allows the response to be shaped as needed with much less compromise in performance. An implementation of the conceptual design, Fig. 3a, is illustrated in Fig. 3b (see details in[9]).
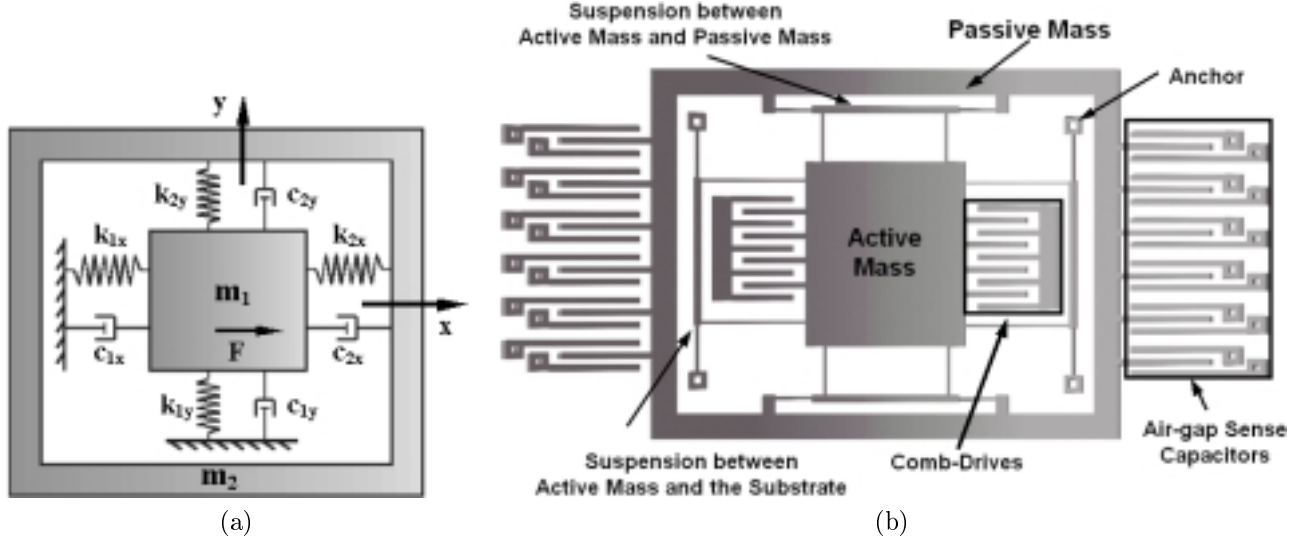

(a)   (b)

Figure 3. (a) Lumped mass-spring-damper model of the dual-mass gyroscope. The first mass is driven in the x direction, and the response of the second mass along the y-axis is sensed. (b) Schematic illustration of a MEMS implementation of dual-mass z-axis gyroscope.

2.1. Principle of Operation

The dynamic system of the proposed micromachined gyroscope consists of the following main components: two vibrating proof masses suspended above the substrate, the flexures between the active mass and the ground which are anchored to the substrate, and the flexures between active mass and the passive mass which mechanically couple the masses (Fig. 3b).

The gyroscope has two orthogonal principle axes of oscillation: the drive direction (x axis in Figure 3a) and the sense direction (y axis in Figure 3a). Both of the proof masses are rendered free to oscillate in the drive and sense directions by the suspension system.

The active mass (m_1 in Figure 3a) is electrostatically forced in the drive direction by the comb-drive structures built on each side of the mass (Fig. 3b). There is no electrostatic force applied on the passive mass (m_2 in Figure 3a), and the only forces acting on this mass are the spring forces and the damping forces. The design approach is based on dynamically amplifying the oscillation of the active mass by the passive mass, as will be explained deeper in the "Dynamic Amplification in Drive Mode" section. The response of the passive mass in the sense direction to the rotation-induced Coriolis force is monitored by the Air-Gap Sense Capacitors built around it (Fig. 3b) providing the angular rate information.

With appropriate selection of dynamical system parameters including the masses and the spring rates, one can obtain the frequency response illustrated in Fig.4. There exists three regions of interest on this response curve: two resonant peaks, regions 1 and 3; and a flat region between the peaks, region 2. The nominal operation of the gyroscope is in the flat region, where the signal gain is relatively high, and the sensitivity of the gain to driving frequency variations is low. Because of the widened bandwidth, a 1% variation in natural frequencies of the system results in only 0.8% error in the output signal, whereas the same fluctuation will produce an error of 20% in the conventional micromachined gyroscopes.[4]
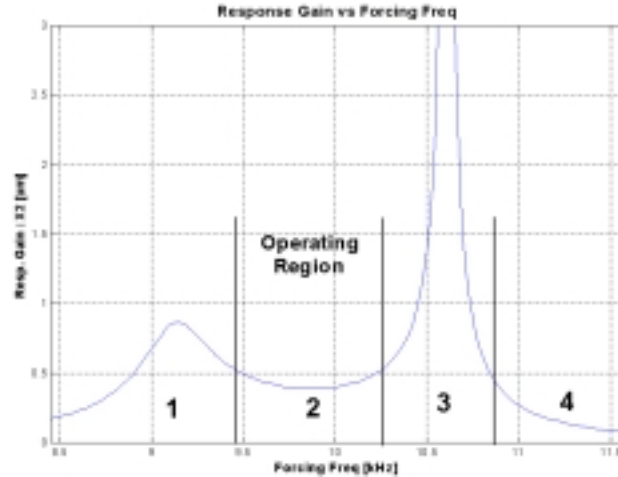
Figure 4. Response of the dual-mass gyroscope in the flat operation region is insensitive to resonant frequency fluctuations and has over 15 times wider bandwidth than existing gyroscopes.
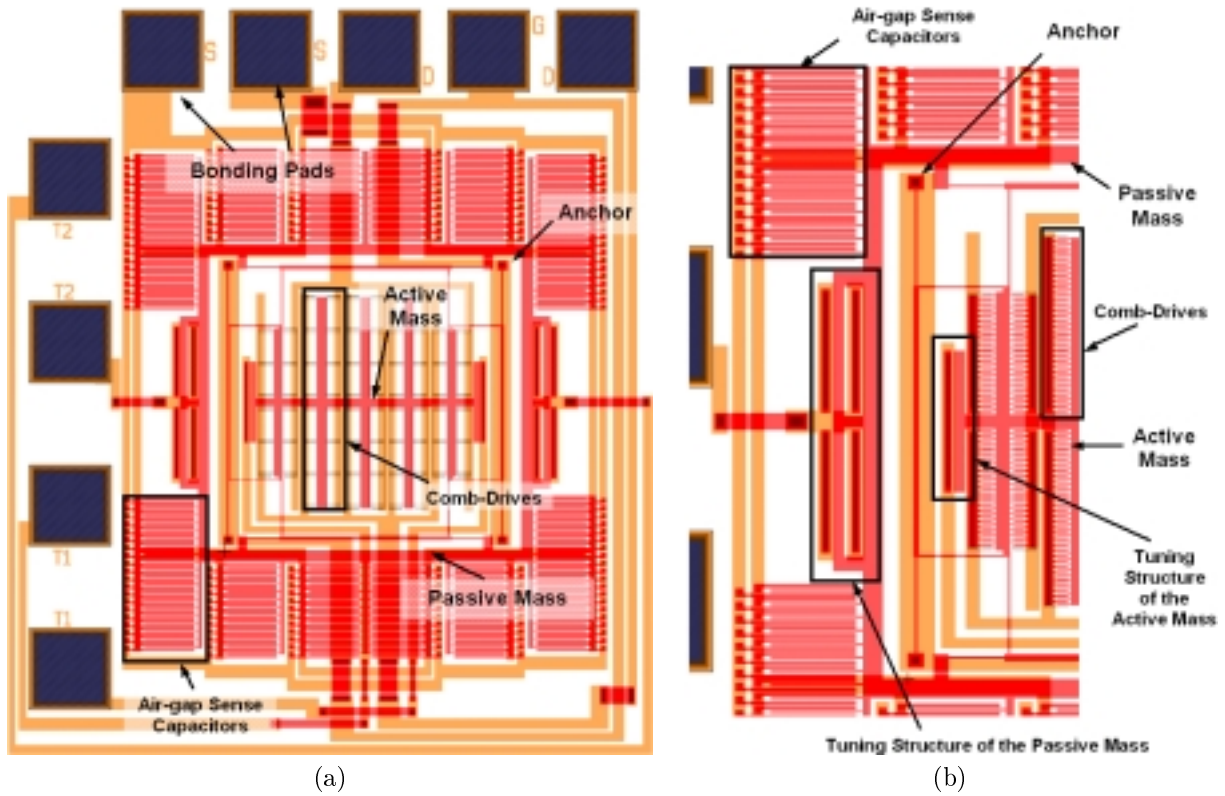

Figure 5. The layout of the dual-mass z-axis gyroscope.

3. IMPLEMENTATION OF THE DESIGN CONCEPT

3.1. Suspension Design

The complete suspension system consists of two sets of four flexible beams per each mass. For each proof mass, one set of fixed-guided beams provides the desired spring rate in the drive direction, while the other set provides the desired spring rate in the sense direction.[9] For a single fixed-guided beam, the translational stiffness in the orthogonal direction to the axis of the beam is given by[10]
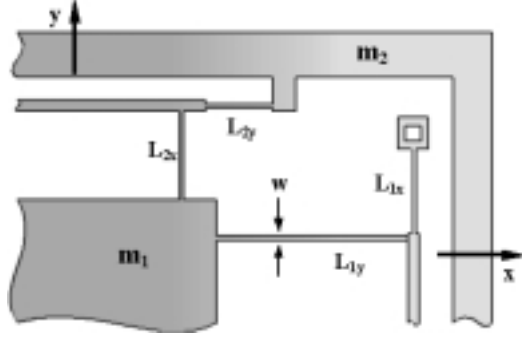
Figure 6. Suspension system configuration provides two degrees of freedom (in drive and sense directions) for the active proof mass and the passive proof mass.

$$k_y = \frac{1}{2}\frac{3EI}{\frac{L^3}{2}} = \frac{Etw^3}{L^3}$$

where E is the Young's Modulus, I is the second moment of inertia, and the beam length, thickness, and width are L, t, w, respectively.

Spring rates for a mass in drive or sense direction are determined by four fixed-guided beams if the axial strains in the other beams are neglected. Thus, each stiffness value in the dynamic system can be calculated as

$$k_{1x} = \frac{4Etw^3}{L_{1x}^3} \ , \ k_{1y} = \frac{4Etw^3}{L_{1y}^3} \ , \ k_{2x} = \frac{4Etw^3}{L_{2x}^3} \ , \ k_{2y} = \frac{4Etw^3}{L_{2y}^3}$$

where w and t are the width and thickness of the beam elements in the suspension, respectively. The individual beam lengths are shown in Figure 6. Finite element analysis of the gyroscope is performed using the software package ANSYS to validate the assumptions in the theoretical analysis. The resonant frequencies obtained from modal analysis results matched the theoretical calculations within 0.1% error. Furthermore, the operational resonant modes were observed to be well separated from the other resonant modes.
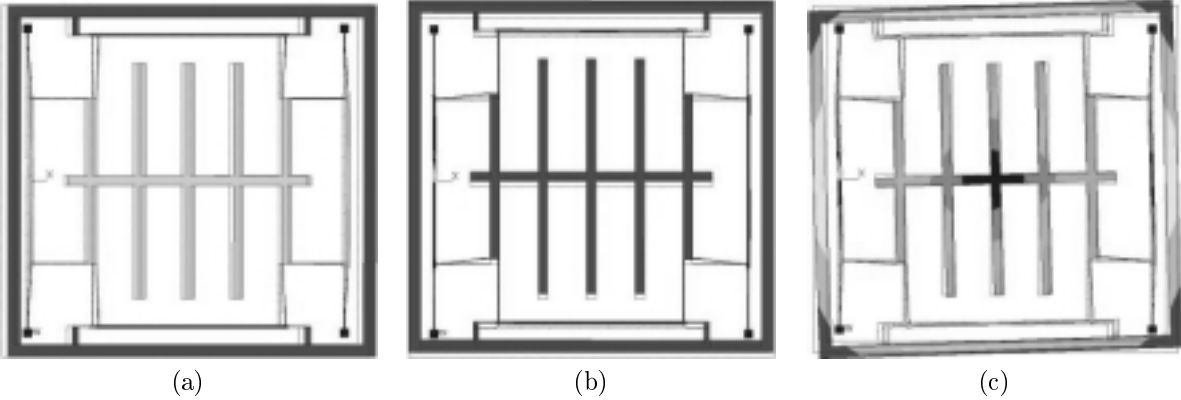

(a)   (b)   (c)

Figure 7. The first three resonant modes of the gyroscope. The simulation is performed using the finite element analysis package ANSYS. FEA results were observed to agree with the theoretical analysis. In addition, non-operational resonant modes were obtained, and were observed to be at significantly higher frequencies.

3.2. Damping Estimation

The four damping coefficients (c_{1x}, c_{1y}, c_{2x}, and c_{2y}) in the dynamical system shown in Figure 3a are due to the viscous effects of the air between the masses and the substrate, and in between the comb-drive and sense capacitor fingers. For the active mass, the total damping in the drive mode can be expressed as the sum of damping due to Couette flow between the mass and the substrate, and the damping due to Couette flow between the integrated comb fingers[2]:

$$c_{1x} = \mu_p p \frac{A_1}{z_0} + \mu_p p \frac{2 N_{comb} l_{comb} t}{y_{comb}}$$

where A_1 is the area of the active mass, z_0 is the elevation of the proof mass from the substrate, t is the thickness of the structure, N_{comb} is the number of comb-drive fingers, y_{comb} is the distance between the fingers, l_{comb} is the length of the fingers, p is the ambient pressure within the cavity of the packaged device, and $\mu_p = 3.710^{-4} \frac{kg}{m^2.s.torr}$ is the viscosity constant for air.

In the sense mode, the total damping is the sum of damping due to Couette flow between the proof mass and the substrate, and the Squeeze Film damping between the integrated comb fingers[2]:

$$c_{1y} = \mu_p p \frac{A_1}{z_0} + \mu_p p \frac{7 N_{comb} l_{comb} t^3}{y_{comb}^3}$$

However, for the passive mass, the total damping in the drive mode results from Couette flow between the mass and the substrate, as well as Couette flow between the air-gap capacitor fingers[2]:

$$c_{2x} = \mu_p p \frac{A_2}{z_0} + \mu_p p \frac{2 N_{capacitor} l_{finger} t}{y_{capacitor}}$$

where A_2 is the area of the passive mass, $N_{capacitor}$ is the number of air-gap capacitors, $y_{capacitor}$ is the distance between the capacitor fingers, and $l_{capacitor}$ is the length of the fingers.

Damping of the passive mass in the sense mode can be estimated as the combination of Couette flow between the proof mass and the substrate, and the Squeeze Film damping between the air-gap capacitor fingers[2]:

$$c_{2y} = \mu_p p \frac{A_2}{z_0} + \mu_p p \frac{7 N_{capacitor} l_{finger} t^3}{y_{capacitor}^3}$$

These pressure dependent effective damping values will be used in the parametric sensitivity analysis simulations of the dynamic system.

3.3. Dynamic Amplification in Drive Mode

To achieve the maximum possible response of the gyroscope, amplitude of the drive-direction oscillation of the passive mass should be maximized. In the drive mode, the dynamic system is simply a 2-DOF system. A sinusoidal force is applied on the active mass by the comb-drive structure. Assuming a lumped parameter model, the equations of motion in the drive mode become:

$$m_1 \ddot{x}_1 + c_1 \dot{x}_1 + (k_1 + k_2) x_1 = F + k_2 x_2$$

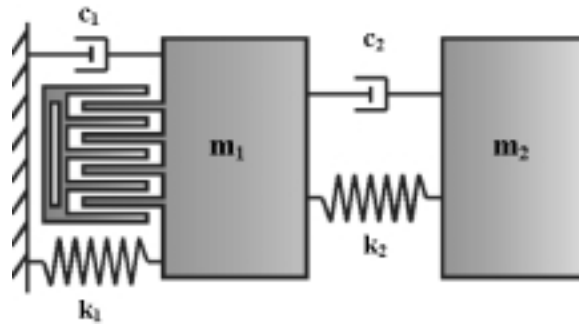$$m_2 \ddot{x}_2 + c_2 \dot{x}_x + k_2 x_2 = k_2 x_1$$

Figure 8. Lumped model of the drive mode of dual-mass gyroscope. The passive mass (m_2) acts as a vibration absorber, to amplify the motion of the active mass (m_1).

When a sinusoidal force $F = F_0 sin(\omega t)$ is applied on the active mass by the interdigitated comb-drives, the steady-state response of the 2-DOF system will be

$$X_1 = \frac{F_0}{k_1} \frac{1 - (\frac{\omega}{\omega_2})^2 + j\omega\frac{c_2}{k_2}}{[1 + \frac{k_2}{k_1} - (\frac{\omega}{\omega_1})^2 + j\omega\frac{c_1}{k_1}][1 - (\frac{\omega}{\omega_2})^2 + j\omega\frac{c_2}{k_2}] - \frac{k_2}{k_1}}$$

$$X_2 = \frac{F_0}{k_1} \frac{1}{[1 + \frac{k_2}{k_1} - (\frac{\omega}{\omega_1})^2 + j\omega\frac{c_1}{k_1}][1 - (\frac{\omega}{\omega_2})^2 + j\omega\frac{c_2}{k_2}] - \frac{k_2}{k_1}}$$

where $\omega_1 = \sqrt{\frac{k_1}{m_1}}$ and $\omega_2 = \sqrt{\frac{k_2}{m_2}}$ are the resonant frequencies of the isolated active and passive mass-spring systems, respectively. When the driving frequency ω_{drive} is matched with the resonant frequency of the isolated passive mass-spring system, i.e. $\omega_{drive} = \sqrt{\frac{k_{2x}}{m_2}}$, the passive mass moves to exactly cancel out the input force F applied on the active mass, and maximum dynamic amplification is achieved.[7]
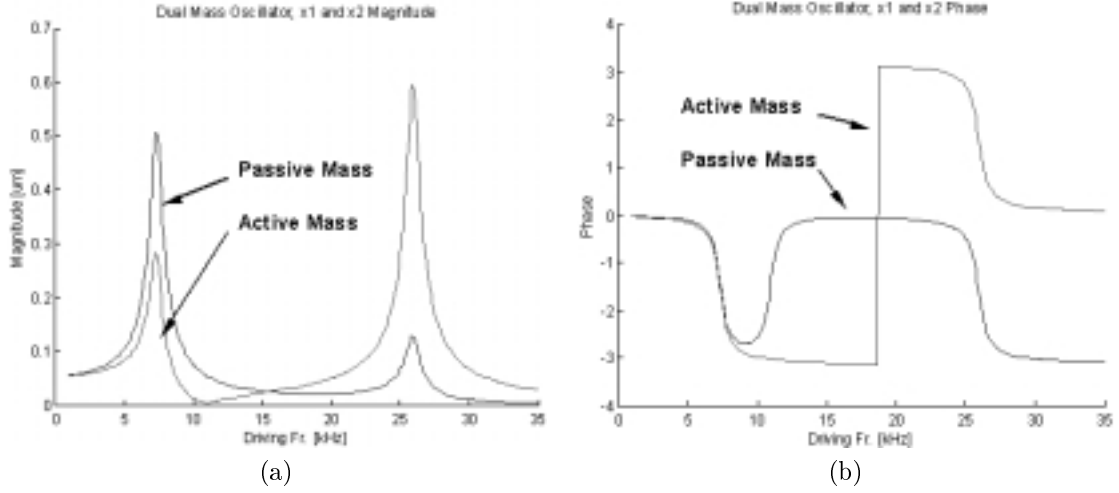

(a)   (b)

Figure 9. (a) The magnitude plots of each proof mass. At the antiresonant frequency, which is the resonant frequency of the isolated passive mass-spring system, oscillation amplitude of the active mass approaches to zero. (b) The phase plots of each proof mass.
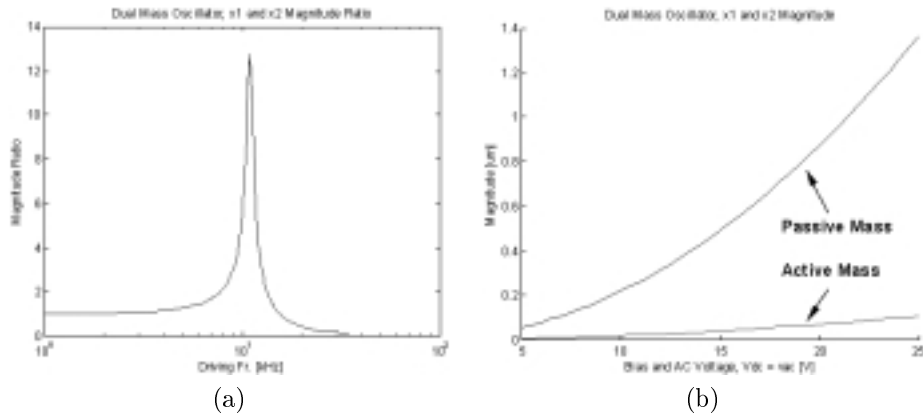

(a)   (b)

Figure 10. (a) The dynamic amplification ratio reaches its maximum at the antiresonant frequency, i.e., $\omega_{drive} = \sqrt{\frac{k_{2x}}{m_2}}$. (b) With a balanced interdigitated comb-drive scheme, a 1 um amplitude is achieved by the passive mass with a bias voltage of about 20V.

The drive-direction oscillation amplitude values can be calculated knowing the magnitude of sinusoidal force $F = F_0 sin(\omega t)$ applied on the active mass by the comb-drive structure. Applying $V_1 = V_{DC} + \nu_{AC}$ to one set of comb drives (e.g. the set on the right side in Fig. 3b), and $V_2 = V_{DC} - \nu_{AC}$ to the opposing set (the set on the left side), a balanced interdigitated comb-drive scheme can be imposed. With this driving scheme, the resulting net electrostatic force is linear to ν_{AC}, which will lead to simplification of the dynamic model:

$$F = 4\frac{\varepsilon_0 z_0 N}{y_0} V_{DC} \nu_{AC}$$

where $\nu_{AC} = |\nu_{AC}|sin\omega t$ is the sinusoidal voltage, V_{DC} is the constant bias voltage, z_0 is the finger thickness, and y_0 is the finger separation. Thus, for the gyroscope, the magnitude of the applied drive force is simply

$$F_0 = 4\frac{\varepsilon_0 z_0 N}{y_0} V_{DC} |\nu_{AC}|.$$

4. DYNAMICS OF THE GYROSCOPE

The dynamics of the gyroscope should be considered in the non-inertial frame. The expression of absolute acceleration (in the inertial frame) of a rigid body with the position vector $\vec{r}$ attached to a rotating reference frame B is:

$$\vec{a_A} = \vec{a_B} + \vec{\Omega}\mathrm{x}\vec{r_B} + \vec{\Omega}\mathrm{x}(\vec{\Omega}\mathrm{x}\vec{r_B}) + 2\vec{\Omega}\mathrm{x}\vec{v_B}$$

where the subscript A denotes "relative to inertial frame A", B denotes "relative to rotating gyroscope frame B", $\vec{v_B}$ and $\vec{a_B}$ are the velocity and acceleration vectors with respect to the reference frame respectively, $\vec{\Omega}$ is the angular velocity of the gyroscope frame, and the operation "x" refers to cross-product. The reference rotating gyroscope frame is assumed to be non-accelerating. The last term $2\vec{\Omega}\mathrm{x}\vec{v_B}$ in the equation, the Coriolis term, is of special interest since the operation of the gyroscope depends on excitation of system in the sense direction by the Coriolis force due to this term. Thus for a mass driven into oscillation in x-direction, and subject to an angular rate of Ω_z about the z-axis, the Coriolis acceleration induced in the y-direction reduces to

$$a_y = 2\Omega_z \dot{x}(t)$$

Similarly, when the active and passive masses are observed in the non-inertial rotating frame, the "gyroscope frame", additional inertial forces appear acting on both masses. The equations of motion for the two-mass system can be written as:

$$m_1\vec{a_1} = \vec{F_{2-1}} + \vec{F_{s-1}} - 2m_1\vec{\Omega}\mathrm{x}\vec{v_1} - m_1\vec{\Omega}\mathrm{x}(\vec{\Omega}\mathrm{x}\vec{r_1}) - m_1\dot{\vec{\Omega}}\mathrm{x}\vec{r_1}$$

$$m_2\vec{a_2} = \vec{F_{1-2}} + \vec{F_{s-2}} - 2m_2\vec{\Omega}\mathrm{x}\vec{v_2} - m_2\vec{\Omega}\mathrm{x}(\vec{\Omega}\mathrm{x}\vec{r_2}) - m_2\dot{\vec{\Omega}}\mathrm{x}\vec{r_2}$$

where $\vec{r_1}$ and $\vec{r_2}$ are the position vectors, $\vec{v_1}$ and $\vec{v_2}$ are the velocity vectors of the masses defined in the gyroscope frame, $\vec{F_{2-1}}$ and $\vec{F_{1-2}}$ are the opposing coupling forces between the masses that each mass applies on other depending on relative position $\vec{r_2} - \vec{r_1}$, including spring and damping forces. $\vec{F_{s-1}}$ consists of spring and damping forces between the active mass and the substrate, and $\vec{F_{s-2}}$ includes the passive mass - substrate damping force. Since both masses are subject to an angular rate of Ω_z about the axis normal to the plane of operation (z-axis), the equations of motion along the x-axis and y-axis become:
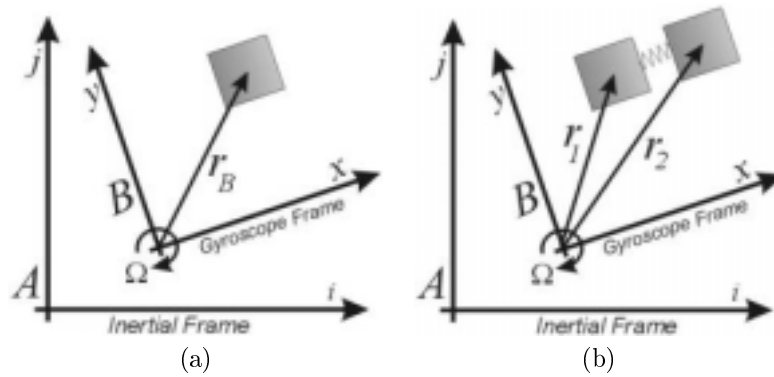

(a)   (b)

Figure 11. (a) Representation of the position vector of a body relative to the rotating frame. (b) Representation of the position vectors of the proof masses of the gyroscope relative to the rotating "gyroscope frame" B.

$$m_1\ddot{x}_1 + c_{1x}\dot{x}_1 + k_{1x}x_1 = k_{2x}(x_2 - x_1) + c_{2x}(\dot{x}_2 - \dot{x}_1) + m_1\Omega^2 x_1 - 2m_1\Omega\dot{y}_1 + m_1\dot{\Omega}y_1 + F_d(t)$$

$$m_2\ddot{x}_2 + c_{2x}(\dot{x}_2 - \dot{x}_1) + k_{2x}(x_2 - x_1) = m_2\Omega^2 x_2 - 2m_2\Omega\dot{y}_2 + m_2\dot{\Omega}y_2$$

$$m_1\ddot{y}_1 + c_{1y}\dot{y}_1 + k_{1y}y_1 = k_{2y}(y_2 - y_1) + c_{2y}(\dot{y}_2 - \dot{y}_1) + m_1\Omega^2 y_1 + 2m_1\Omega\dot{x}_1 + m_1\dot{\Omega}x_1$$

$$m_2\ddot{y}_2 + c_{2y}(\dot{y}_2 - \dot{y}_1) + k_{2y}(y_2 - y_1) = m_2\Omega^2 y_2 + 2m_2\Omega\dot{x}_2 + m_2\dot{\Omega}x_2. \tag{1}$$

where $F_d(t)$ is the driving electrostatic force applied to the active mass, and Ω is the angular velocity applied to the gyroscope about the z-axis.

The overall dynamic model can be reduced having the active mass driven into forced oscillation in drive direction by $F_d(t)$ with a constant amplitude x_o and a frequency ω_d. Assuming the oscillation of the first mass in the drive direction is set by the control system to be

$$x_1 = x_o cos(\omega_d t),$$

the system (1) reduces to 3 degrees of freedom. The equations of motion of the reduced system become[4]:

$$\ddot{y}_1 + 2\omega_n\xi\dot{y}_1 + 2\mu\omega_n\xi(\dot{y}_1 - \dot{y}_2) + (\omega_n - \Omega)y_1 + \omega_n^2\sigma_1(y_1 - y_2) = -2\Omega\omega_d x_o sin\omega_d t + \dot{\Omega}x_o cos\omega_d t$$

$$\beta(\ddot{y}_2 - \Omega^2 y_2) + 2\mu\omega_n\xi(\dot{y}_2 - \dot{y}_1) - 2\beta\Omega\dot{x}_2 - \beta\dot{\omega}_z x_2 + \omega_n^2\sigma_1(y_2 - y_1) = 0$$

$$\beta(\ddot{x}_2 - \Omega^2 x_2) + 2\beta\Omega\dot{y}_2 + \beta\dot{\Omega}y_2 + \omega_n^2\sigma_2 x_2 = w_n^2\sigma_2 x_o cos\omega_d t \tag{2}$$

where $\beta = m_2/m_1$, $\sigma_1 = k_{2y}/k_{1y}$, $\sigma_2 = k_{2x}/k_{1x}$, $\mu = c_2/c_1$, $\xi = c_1/(2m_1 w_n)$, and w_n is the natural frequency in the sense direction .

5. PARAMETRIC SENSITIVITY ANALYSIS

5.1. Fabrication Variations

Fabrication variations can affect the parameters of gyroscopes directly. For micromachining processes, the dimensions of the suspension beam elements are uncertain for different reasons. The length of the beams are determined solely by lithography, and are extremely accurate. However, the thickness is determined by deposition process, and the width set by lithography is affected by etching process. Thus, these two parameters are less accurate, and can vary by 1% from wafer to wafer.

In conventional gyroscopes, fabrication variations result in resonant frequency shifts, requiring compensation by sophisticated control electronics. Yet, for the proposed system, a 0.05 μm deviation from 2 μm nominal beam width or a 0.1 μm deviation from 2 μm nominal structure thickness results in less than 1% error in the gain (Fig. 12a and 12b, respectively). Moreover, a variation in deposition conditions that affect the Young's Modulus of the gyroscopes structure by 10 GPa causes less than 0.5 % error (Fig. 12c). The same parameter variations in a conventional micromachined gyroscope without compensation by control system result in over 10% error.

5.2. Pressure Fluctuations

Pressure fluctuations can have significant effects on resonance dependent conventional gyroscopes (Fig. 2). However, since the proposed device utilizes dynamic amplification of mechanical motion, and does not operate in resonance, the response is insensitive to damping changes in the operation region. For a possible vacuum leakage from 100 militorrs to 500 militorrs, e.g. due to package sealing defects over the operation time of the device, the response gain reduces by less than 2% (Fig. 12d), where the same pressure variation can result in over 20% gain reduction in a conventional gyroscope design.
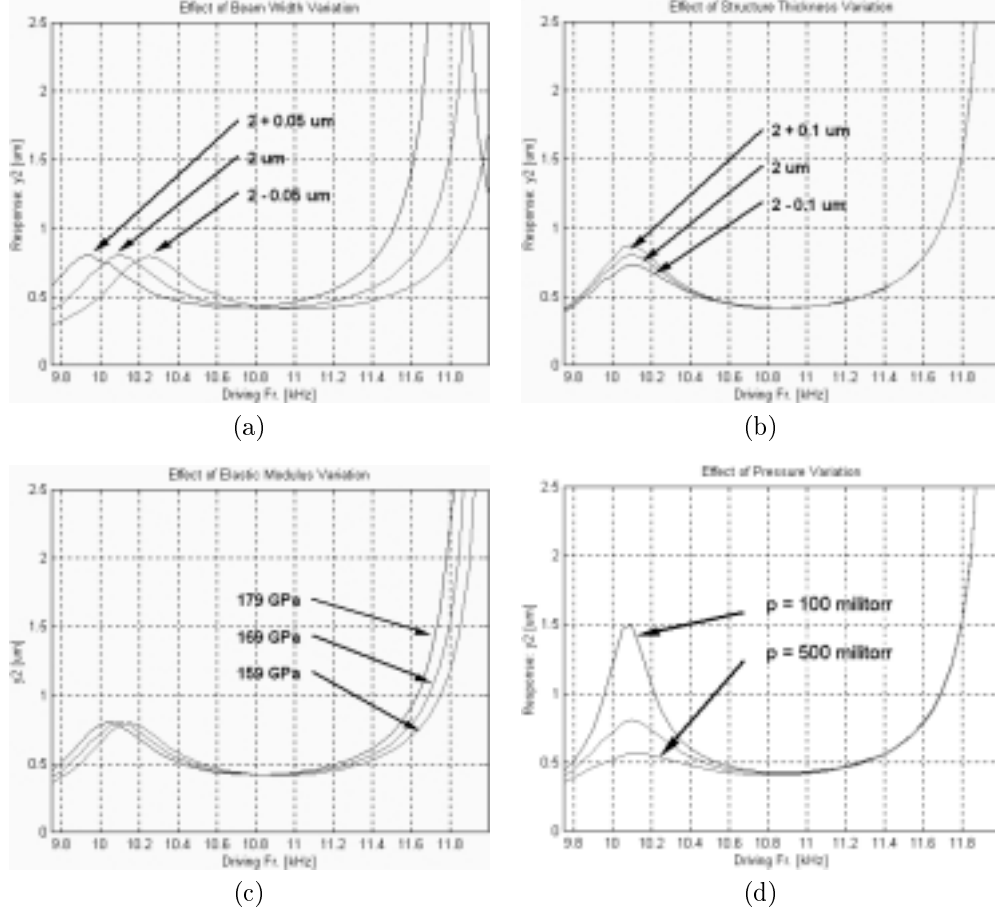
Figure 12. Change in the response due to: (a)$0.05\mu m$ variation in the width of suspension beams, (b)$0.1\mu m$ variation in structure thickness, (c)10 GPa variation in Young's Modulus, (d) ambient pressure change form 100 militorrs to 500 militorrs.

5.3. Thermal Fluctuations

Variations in the temperature of the structure can perturb the dynamical system parameters by three means: due to the inherent temperature dependence of Young's Modulus, due to changes in suspension geometry because of thermal expansion, and due to the thermally induced localized stress effects. Young's modulus of the structure at a given temperature can be calculated by[8]:

$$E_{0^\circ C + \Delta T} = E_{0^\circ C} TC_E \Delta T + E_{0^\circ C}$$

where $E_{0^\circ C}$ is the Young's modulus for fine-grained polysilicon at 0 °C (assumed 169 GPa), TC_E is the temperature coefficient of Young's modulus for polysilicon (assumed[8] -75 ppm/°C), and ΔT is the temperature change. To reflect the effects of temperature dependent elastic modulus and thermal expansion on the resonant frequency of linear microresonators with folded-beam suspensions, the temperature coefficient of the resonance frequency can be determined as[8]:

$$TC_f = \tfrac{1}{2}(TC_E - TC_h)$$

where TC_E is the temperature coefficient of the Young's modulus, and TC_h is the temperature coefficient of thermal expansion, which is assumed 2.5 ppm/°C; leading to a perturbed resonant frequency of

$$\omega_{n_{0^\circ C + \Delta T}} = \omega_{n_{0^\circ C}} TC_f \Delta T + \omega_{n_{0^\circ C}}$$

However, for the proposed suspension system, more accurate results can be found conducting finite element analysis of the system. To be able to capture parameter changes due to the temperature dependence of Young's Modulus, due to thermal expansion generated alteration in suspension geometry, and due to thermally induced stresses; a finite element model of the device was created using the finite element analysis software package ANSYS. First, a uniform temperature loading of $100°C$ was applied to each surface, and the thermally induced localized stresses were observed. The results of the thermal finite element simulation indicated that a stress of 82 MPa was induced only in the drive-direction beam elements of active mass, effecting only k_{1x}. The other beam elements of the suspension system were observed stress-free (Figure 13a). Then static structural analysis of the thermally loaded system with the modified Young's modulus was performed to calculate each of the four spring rates (k_{1x}, k_{1y}, k_{2x}, and k_{2y}) in the dynamical system shown in Figure 3a. The same procedure was also carried out for a uniform temperature loading of $-100°C$. The simulation of the dynamical system with the perturbed parameters due to thermal loading indicated an deviation of less than 0.9% in the gain. Finite element analysis of a conventional gyroscope with similar geometry demonstrated about 7% gain error for the same thermal loading.
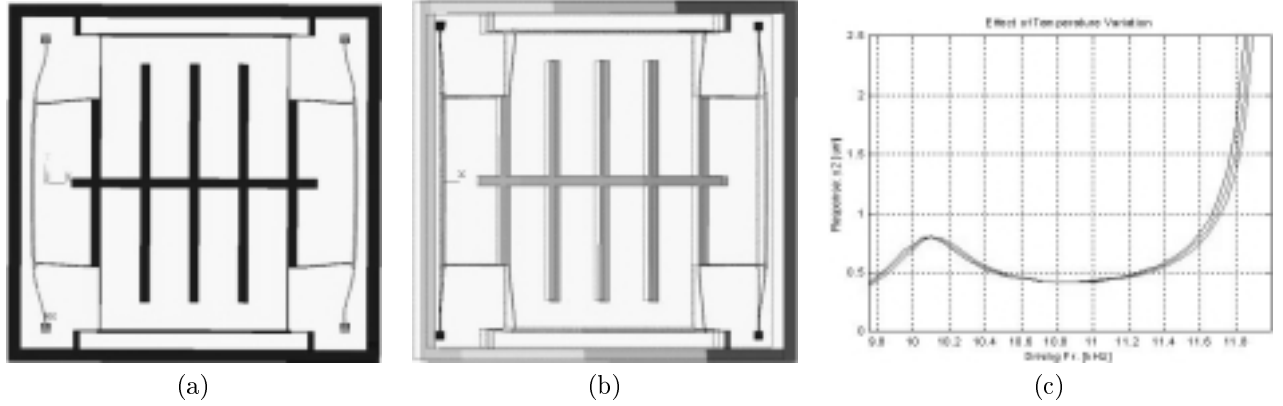

(a)   (b)   (c)

Figure 13. (a) Finite element simulation of the device with a uniform temperature loading of $100°C$. Thermally induced localized stresses were observed only in the drive-direction beam elements of active mass, effecting only k_{1x}. (b) Static finite element analysis of the thermally loaded system with the modified Young's modulus. (c) Simulation of the dynamical system with the perturbed parameters due to thermal loading was performed, indicating less than 0.9% gain deviation.

5.4. Residual Stresses

Accumulation of residual stresses in the structure directly affect the properties of the dynamical system. In the presence of residual stresses, the beam stiffness values, and thus the overall system spring rates change. Axial residual stresses in x direction effect only the y-direction spring rates (k_{1y} and k_{2y}) of the suspension, while axial residual stresses in y direction effect only the x-direction spring rates (k_{1x} and k_{2x}).

Thus, for the suspension system with an x-direction axial residual stress of ε_x and a y-direction axial residual stress of ε_y, the spring rate values become[3]

$$k_{1x} = \frac{Etw\kappa_y^2}{12L_{1x}}[1 - \frac{2w}{\beta_{1x}L_{1x}}\frac{cosh(\frac{\kappa_y L_{1x}}{w})-1}{sinh(\frac{\kappa_y L_{1x}}{w})}]^{-1} \ ,$$

$$k_{1y} = \frac{Etw\kappa_x^2}{12L_{1y}}[1 - \frac{2w}{\beta_{1y}L_{1y}}\frac{cosh(\frac{\kappa_x L_{1y}}{w})-1}{sinh(\frac{\kappa_x L_{1y}}{w})}]^{-1} \ ,$$

$$k_{2x} = \frac{Etw\kappa_y^2}{12L_{2x}}[1 - \frac{2w}{\beta_{2x}L_{2x}}\frac{cosh(\frac{\kappa_y L_{2x}}{w})-1}{sinh(\frac{\kappa_y L_{2x}}{w})}]^{-1} \ ,$$

$$k_{2y} = \frac{Etw\kappa_x^2}{12L_{2y}}[1 - \frac{2w}{\beta_{2y}L_{2y}}\frac{cosh(\frac{\kappa_x L_{2y}}{w})-1}{sinh(\frac{\kappa_x L_{2y}}{w})}]^{-1} \ .$$

where $\kappa_y = \sqrt{12\varepsilon_y}$, $\kappa_y = \sqrt{12\varepsilon_y}$ are the dimensionless strain factors for beam bending, and $\beta_{1x} = \frac{L_{1x}w}{\kappa_y}$, $\beta_{1y} = \frac{L_{1y}t}{\kappa_x}$, $\beta_{2x} = \frac{L_{2x}w}{\kappa_y}$, $\beta_{2y} = \frac{L_{2y}t}{\kappa_x}$.

However, an axial residual stress ε_x in the x direction effect the sense-direction spring rates (k_{1y} and k_{2y}) of the same order, and an axial residual stress ε_y in the y direction effect the drive-direction spring rates (k_{1x} and

k_{2x}) of the same order as well. In result, the overall system response is less sensitive to residual stresses (Fig. 14). To compare the sensitivity of the proposed device to the conventional approach, the designed system and a single mass gyroscope with the same geometry of the isolated active mass-spring system were simulated with a 10 MPa compression residual stress. The single-mass system experienced approximately 2.5% gain reduction, while the proposed device experienced less than 0.2% deviation in the gain.
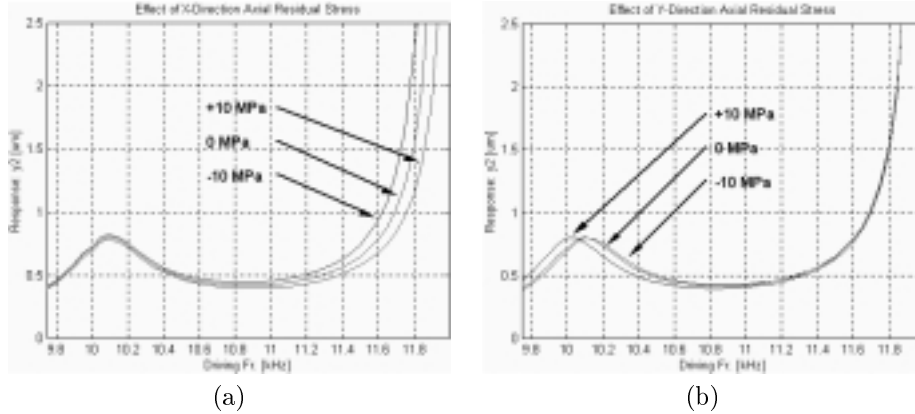

$$(a) \qquad\qquad\qquad\qquad (b)$$

Figure 14. Effect of residual stresses (a) in x-direction, (b) in y-direction.

6. CONCLUSION

A new micromachined gyroscope design with inherent disturbance-rejection is presented, the dynamical system and the design implementation are analyzed, and effects of realistic parameter variations on the system response are investigated. The implementation of the idea is based on the use of two independently oscillating proof masses. By utilizing dynamical amplification, the necessity of operation in the resonance mode is eliminated, and over 15 times increase in the bandwidth of the system is achieved. The proposed device is demonstrated to have improved robustness against expected fabrication and packaging fluctuations, especially against damping variations due to ambient pressure, compared to the conventional micromachined gyroscopes. Sensitivity analysis revealed that, for the same thermal loading, the device produces 87% less error than conventional gyroscopes. Moreover, the proposed design was shown to be approximately 12 times less sensitive to residual stresses, and 20 times less sensitive to fabrication variations than conventional gyroscopes. Consequently, with the presented design approach, tight fabrication tolerances and packaging requirements can be relaxed resulting in a lower production cost of MEMS gyroscopes.

REFERENCES

1. N. Yazdi, F. Ayazi, and K. Najafi. Micromachined Inertial Sensors. *Proc. of IEEE, Vol. 86, No. 8*, August 1998.
2. W.A. Clark. Micromachined Vibratory Rate Gyroscope. *Ph.D. Thesis, BSAC, U.C. Berkeley*, 1994.
3. W.A. Clark, R.T. Howe, and R. Horowitz. Surface Micromachined Z-Axis Vibratory Rate Gyroscope. *Proceedings of Solid-State Sensor and Actuator Workshop*, June 1994.
4. E. Netzer, and I. Porat. A Novel Vibratory Device for Angular Rate Measurement. *Journal of Dynamic Systems, Measurement and Control*, Dec. 1995.
5. A. Shkel, R.T. Howe, and R. Horowitz. Micromachined Gyroscopes: Challenges, Design Solutions, and Opportunities. *Int. Workshop on Micro-Robots, Micro-Machines and Systems, Moscow, Russia*,1999.
6. A. Shkel, R. Horowitz, A. Seshia, S. Park and R.T. Howe. Dynamics and Control of Micromachined Gyroscopes *American Control Conference, CA* ,1999.
7. C.W. Dyck, J. Allen, R. Hueber. Parallel Plate Electrostatic Dual Mass Oscillator. *Proceedings of SPIE SOE, CA*, 1999.
8. L. Lin, R.T. Howe, and A.P. Pisano. Microelectromechanical Filters for Signal Processing. *Journal of Microelectromechanical Systems, Vol. 7*, Sept. 1998.
9. C. Acar and A. Shkel. Wide Bandwidth Micromachined Gyroscope to Measure Rotation. *Patent pending, UCI Office of Technology Alliances*, Case No:2001-140-1.
10. W.C. Young. Roark's Formulas for Stress & Strain. *McGraw-Hill, Inc.*, 93-156, 1989.